PCCP

PAPER

View Article Online
View Journal | View Issue

Cite this: *Phys. Chem. Chem. Phys.*, 2025, **27**, 25569

Condensed and gaseous benzonitrile: ionic species formation and structural parameters

Jorge H. C. Basilio, [a] Ricardo R. Oliveira, *[b] Roberto Nascimento, [a] Maria Luiza M. Rocco, [b] Lucia H. Coutinho, [a] Fabio de A. Ribeiro [c] and Wania Wolff *[a]

Received 5th September 2025,
Accepted 25th October 2025

DOI: 10.1039/d5cp03437j

rsc.li/pccp

Laboratory experiments were performed to evaluate benzonitrile (CN–Bz) under electron impact in the condensed phase by electron-stimulated ion desorption (ESID) and in the gas phase by ionization time of flight mass spectrometry with high mass resolution (EI-TOF-MS). This report focuses on the identification and quantification of the single and double charged ionic species from small to large masses initiated by radiolysis in the electron impact range of 12 eV to 2000 eV and desorption at 2300 eV electrons. The fragmentation of isolated CN–Bz in the gas phase is compared with the ejection of positive ions from the surface of condensed CN–Bz. The results highlight the dissociation, isomerization and formation of larger molecules and double charged metastable species. On the theoretical side, an automated global minimum (GM) search for low energy isomers was performed for selected ionic and dicationic species suggesting possible structures. Harmonic frequency calculations ensured that all structures represented a minimum at the potential energy surface. Based on data collected by spacecraft missions sent to the Saturn moon Titan, the presence of benzonitrile in the Titan atmosphere is discussed and suggests a low survival lifetime of the gaseous molecule at high altitudes, but its possible formation in haze aerosols.

1. Introduction

Organic molecules containing a cyano group became important in response to the detection of benzene and large nitriles in molecular clouds and protostars.[1–6] The reaction between benzene and the CN radical can form CN–Bz.[7–10] Benzene is the most well-known aromatic hydrocarbon identified in astrophysical environments. Species much larger than benzene have gained relevance since the detection of high masses of up to 300 Daltons in the upper atmosphere of Titan[11] and recently in Mars.[12] Small nitriles, such as HCN, CH_3CN, HC_3N, C_2N_2, were detected in the stratosphere and larger ones in the ionosphere, such as butyne-dinitrile ($C_4H_4N_2$) and propanenitrile (C_2H_5CN).[13–15] Benzene and some derivatives that possess stable electronic states have shown measurable intensities.[16,17] Some other dicationic species are listed in Table S1 (SI). N_2^{2+}, which has a very high life expectancy,[18,19] and N_2O^{2+} have been suggested to be present in the upper atmosphere of Titan.[20–23]

Recently, electron impact experiments were performed at 15–50 eV[24] and 70 eV.[25] The former work shows that the dissociative ionization of benzonitrile produced high intensity ions with m/z = 75, 76, 77 and 102, corresponding to C_2H_4/H_2CN, HCN/HNC, C_2H_2/CN and H-loss, respectively. The latter study observed that metastable dissociative ionization becomes important when ionization occurs with significant excess energy transfer. For example, $C_4H_2^+$ can be formed through sequential dissociation *via* the excitation of $C_6H_4^+$ and $C_6H_5CN^+$. Previous electron impact experiments, photoionization and multi-photon ionization investigations primarily focused on direct HCN loss and ion species that contribute to the formation of larger interstellar molecules.[26–31]

Photochemical models were developed considering the chemical pathways and mechanisms that can lead to the formation and destruction of aromatic and cyano species.[32–37] Theoretical works from a gas–grain kinetic chemical model NAUTILUS[38] and experimental data[7,39] established that the formation of CN–Bz from the radical benzene and CN is efficient under interstellar conditions.[8,39]

First, we present an experimental investigation on the ionization and fragmentation of CN–Bz in the gas phase over a wide energy range (12–2000 eV), allowing us to follow the cross-section dependence of several ionic species (positive ions, single and double charged) as a function of the impact energy from near threshold energies to energetic 2000 eV electrons. An absolute cross-section of single and double species is always

[a] *Physics Institute, Federal University of Rio de Janeiro, Rio de Janeiro, Brazil. E-mail: wania@if.ufrj.br*
[b] *Chemistry Institute, Federal University of Rio de Janeiro, Rio de Janeiro, Brazil. E-mail: rrodrigues.iq@gmail.com*
[c] *Federal Institute of Rio de Janeiro, Nilópolis, RJ 26530-060, Brazil*

needed for data simulation. The formation and destruction rate constants of positive ions can be derived (see Table S2 and Fig. S18 in the SI). The data were further applied to the chemistry of the atmosphere of Saturn's moon Titan. In the condensed phase experiments, energetic electrons at 2300 eV were impinged on thin icy films. The primary comparison was done with data in the gaseous phase, but the main goal was to identify differences in the ejection of ionic species from the surface upon slightly heating the sample and sublimating a few layers of films. The condition for the highest production of molecules larger than that of protonated benzonitrile was searched for.

On the theoretical side, for selected single and double charged ionic species, low-energy isomers were calculated on the basis of an automated global minimum (GM) search. Harmonic frequency calculations show that all structures represent a minimum at the potential energy surface. Looking for more accurate energy results, the optimized geometries were subjected to a CASSCF calculation with total energy obtained *via* the second-order perturbation theory.

This report is divided into the following sections: experimental setup and protocols in gaseous and condensed phases, computational details, results of ionic species in gas and condensed phases, comparison between phases and global minimum structures of aggregates, Astrophysical implications – benzonitrile in the Titan atmosphere, and conclusion.

2. Experimental setup and protocols

2.1. Gaseous phase

The experiments were carried out in an ultrahigh vacuum chamber with a base pressure of 10^{-8} mbar, while the pressure on the reflectron time of flight mass spectrometer (TOF-MS) was 5×10^{-8} mbar. A detailed description of the experimental setup can be found elsewhere;[17] here we include specific features applied for the CN–Bz measurements. The sample pressure in the gas cell, measured by a capacitive sensor, was kept almost constant at 10^{-5} mbar, ensuring a single collision regime. Before the sample was introduced into the gas cell, a background experiment was performed under the same beam conditions. This allowed us to identify contaminant species, predominantly water and molecular hydrogen.

The injection line was heated prior to the admission of the sample for at least 2 hours and dried under argon to reduce contamination by water vapor. The procedure was repeated twice in shorter periods. During the experiments, the injection line was kept at room temperature to maintain constant flow and prevent degassing of the water from the stainless steel tubes.

The liquid CN–Bz sample was purchased from Sigma-Aldrich with purity greater than 99.8%. The dissolved gas trapped within the CN–Bz liquid was removed by repeated freeze–pump–thaw cycles of the sample before admission to the main chamber. Previously, the CN–Bz molecules were dehydrated by adsorption using 4A molecular sieves. The liquid sample was placed in a dry ice–ethanol slush bath at around −10 °C, which freezes only water but not CN–Bz (freezing point: −12.9 °C). This procedure helped us maintain a constant evaporation rate and gas pressure in the cell during the hours of measurements.

High resolution reflectron time-of-flight mass spectrometry permits a high degree of sensitivity to the identification of single- and double-charged atomic and molecular species.[17] The spectrometer mass calibration was done with noble gases neon, argon, krypton and xenon, so that the isotopic components could be discriminated. A pulsed electron gun delivered electrons with energies from 12 to 2000 eV (with an energy resolution of ±2 eV) at a repetition rate of 50 kHz. The ions were collected by a pulsed extraction field applied to the gas cell electrodes. The ions were collected by a 1 μs long extraction pulse of −350 V, applied to the gas cell electrode, transmitted through a reflectron spectrometer, and detected by a dinode detector. The ion count rate was maintained at 1–3 kHz. The average electron beam current, in the nA order, collected by a Faraday cup, and the sample pressure in the cell, were monitored and recorded during the experiments. Several TOF spectra were collected at different energies to define the ionic formation over the electron-energy range of the fluxes measured by the Cassini spacecraft (electron fluxes are shown in Fig. S1).

2.2. Condensed phase

The experimental setup consists of an ultrahigh vacuum chamber maintained at 1.0×10^{-9} mbar base pressure. The instruments housed in the chamber are an XYZ sample manipulator connected to an open cycle liquid nitrogen cooling system, a commercial electron gun (Kimball Physics, ELG-2), a linear time-of-flight mass spectrometer, a quadruple mass spectrometer (RGA), and a pressure gauge sensor. The liquid sample CN–Bz was purchased from Sigma-Aldrich with purity greater than 99.8%. The CN–Bz liquid sample was subjected to the fractional distillation process[40] to separate it from any trace of water (at 100 °C and CN–Bz at 190 °C). After being distilled, it was accommodated into a glass vial and degassed through several freeze–pump–thaw cycles prior to transfer to the main chamber. The controlled-time injection procedure was improved using a LabVIEW monitoring software based on the RGA and the temperature sensor.

The sample holder substrate was mounted on an XYZ manipulator, cooled using an open-cycle liquid nitrogen system. The injection line was heated and dried with nitrogen gas and set at room temperature before injection. When the holder temperature reached its minimum, at 120 K, the CN–Bz ice analogue was grown *in situ* by admission of CN–Bz vapor in the chamber with an ultrafine leak valve at 3.0×10^{-7} mbar for 20 minutes. The sample flux was monitored by software measuring the gas pressures of CN–Bz and the contaminants present in the chamber during the injection time. The thickness of the film was estimated to be ∼6 Langmuir, where 1 Langmuir = 1×10^{-6} Torr s.[41] An admission spectrum is shown in Fig. S1 (in the SI). The substrate temperature and the sample pressure were monitored using an Eurotherm instrument and

an RGA spectrometer, respectively. The LabVIEW platform integrates these two sources of data, enabling the use of the temperature-programmed desorption technique (TPD).

Once the first film was deposited, the TPD technique was applied to evaluate the selected deposition conditions. The quality of the film was probed and the thermal desorption of the film was measured as a function of time. In typical TPD measurements, the sample holder was heated at a controlled rate (0.1 K s), and the ionic CN–Bz fragments were recorded as a function of temperature.

A 1900 V potential was applied to the holder, extracting the ionic species ejected from the sample surface. This positive potential applied to the sample also accelerates the primary 400 eV electrons emitted by the electron gun (energy resolution: of ±2 eV). Therefore, 2300 eV electrons impinge on the sample surface. The gun exit was at a distance of 5 cm from the sample holder, which was placed perpendicular to the spectrometer axis, 1 cm from its entry. The electron beam was focused on a spot size of 0.5 mm^2 and hit the sample at an incidence angle of 60 degrees normal to the surface. After extraction, the positive ions were guided towards the time-of-flight spectrometer through a metallic grid set at 1350 V and traveled through a 25 cm long field-free drift tube (grounded), hitting a set of microchannel plate detectors in chevron configuration. The ion species ejected from the surface of the holder (without the sample) known from previous experiments allowed mass calibration. For consistency, the spectrometer and holder settings were not changed between samples. The preliminary linear regression can then be improved by extending the mass calibration to other peaks that arise in ionic series recognizable in the TOF spectrum of the sample molecule up to and including parent ion peak. From this procedure, the entire TOF spectrum can be converted to the m/z ratio scale.

An external pulse generator (HP 8116A) was responsible for the triggering and pulsing of the electron beam with a signal width of 20 nanoseconds within a time repetition rate of 80 kHz. In the experiments, a beam current of 0.4 nA was used, which delivers a low electron flux of 3×10^4 electrons and a low fluence of 6×10^6, avoiding sample damage. The pulse generator supplies the start signal of the time-to-digital converter device (FastComTec-TDC P8778) that provides a 12.5 μs time window for the arrival of ions. Each ion generates an output MCP signal processed by a preamplifier (Ortec VT120A), with noise discriminated by a Tennelec-CFD, and fed into a gate generator, delivering a NIM signal with 800 ns width, used as the stop signal of the TDC device. The ion count rate with the sample was stabilized at 4–5 kHz.

3. Computational details

For the ionic species $C_6H_5CN^{2+}$, $C_6H_3CN^{2+}$, $C_6H_5CNH^+$, $C_6H_5CHNH^+$ and $C_6H_5CHNH_2^+$, we performed an automated global minimum (GM) search for low-energy isomers. The candidates were identified using the ABCluster software through the isomer module,[42,43] which applies the artificial bee colony algorithm based on swarm optimization (Fig. 1). The isomer module integrates the extended GFN2-xTB tight binding parameterization[44] into the ABCluster main algorithm. For each search, among the 10,000 and 15,000 structures generated, we selected 100 to 150 lowest-energy structures for further computations. For selected cases, some structures were added manually by chemical intuition (Fig. 1). This procedure is recommended due to the large chemical space.[45] All selected structures were then optimized applying density functional theory (DFT), using ORCA 5.4 software[46,47] at the PBE0/def2-TZVP level of theory. This level of theory has been successfully applied in previous works.[17,41,48,49]

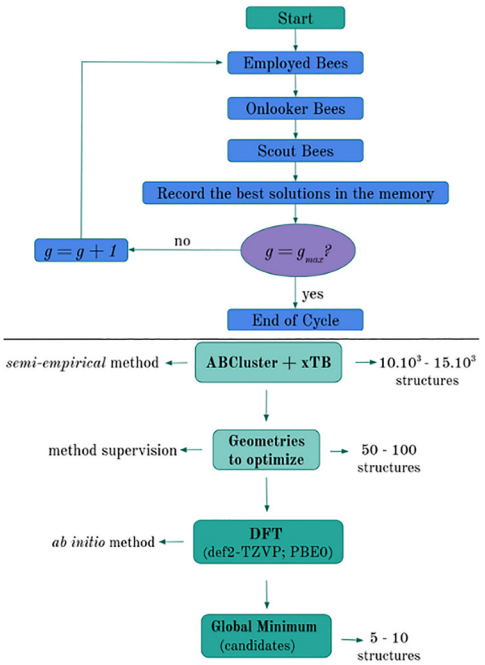

Fig. 1 (Upper) Diagram of the swarm optimization algorithm, which progresses through initialization, exploration by employed bees, selection by onlooker bees, and random search by scout bees, iterating until a stopping condition is met. (Down) Theoretical method workflow, starting with the xTB approach for structure screening, followed by DFT optimization using the PBE0 functional for a computationally efficient *ab initio* method.

In addition, harmonic frequency calculations were performed to ensure that all structures represent a minimum at the potential energy surface (wavenumbers are shown in Tables S3 to S7 in the SI). For more accurate energy results, the optimized geometries were subjected to a couple cluster calculation at the CCSD(T)/cc-pVTZ level to obtain the total energy. The groups of isomers in which at least one of the candidates presented a coupled cluster T1 diagnosis ≥ 0.03[50] were subjected to a CASSCF calculation with total energy obtained *via* the second-order perturbation theory at the NEVPT2/def2-TZVP level of theory. We used the notation $\mathbf{X.Y}^{+/2+}$, where $X = 3$, 5, 6, 7, and 8, representing the number of hydrogen atoms in each group of molecules, and Y = 1, 2, 3, and 4, indicating the stabilization order of relative energies in each group of ionic species.

4. Results

4.1. Ionic species in the gas phase

Fig. 2 presents the mass spectrum of CN–Bz under the impact of 125 eV electrons, around the maximum of absolute cross sections. The spectrum shows that the mass/charge species were discriminated well and structured into eight defined groups labeled A–H.

Each group includes fragments with a specific number of carbon atoms and/or nitrogen atoms attached to hydrogen. A total of 51 ionic species were measured and all major and minor fragment ions were assigned to a molecular ionic radical in Fig. 2. All detected ion species are in agreement with the prompt ions detected from multiphoton ionized benzonitrile.[25] The dominant peak in the spectrum corresponds to the parent ion, and other major fragment ions in descending order are m/z = 76, 50, 39 and 63.

There are no experimental data on the total ionization cross section (TICS) for CN–Bz over a wide energy range; the only data available in the literature are at 70 electron impact.[51,52] As for computed TICS, there are calculations from the ionization threshold to 5000 eV based on the BEB model with various combinations of orbital parameters and the CSP-ic method.[53] The correlation of the calculated TICS and polarizability showed that BEBω B97-X results gave the best comparison with BEB and the CSP-ic method. We opted to normalize the present relative yields in absolute cross sections with the BEB calculation.

Fig. 3 shows the absolute total ionization cross section (TICS), nondissociative single ionization cross section (ICS), dissociative cross section (DCS), and fragment cross section of the relevant ionic species of the ionic groups A–H (see Fig. 2). At low electron impact energies of 12–16 eV, the parent ion and $C_6H_4^+$ (m/z = 76) are mainly formed, the latter with a very low yield. The ionic fragments in this range are produced in minor abundances, in agreement with Fig. S1 of ref. 24. For comparison, the destruction cross-section of CN–Bz is 0.1 Mb at 16 eV (twenty-five times less than TICS), reaches a maximum of 10 Mb at 100 eV, and decays to 1.7 Mb at 2000 eV as shown in Fig. 3 and listed in Table S2 (in the SI).

The metastable doubly charged positive ions $C_6H_n^{2+}$ (n = 4–6) with m/z = 36.5, 37.5, and 38.5 were already reported in a previous work[17] and recently mentioned in ref. 25. We present the ratio of $C_6H_5CN^{2+}$ and $C_6H_3CN^{2+}$ relative to the ionized $C_6H_5CN^+$ (see Fig. 4). The peak at m/z = 51.5 is attributed to benzonitrile dication, $C_6H_5CN^{2+}$, and shows that a small amount is formed under electron impact, with the ratio reaching 4%. The less intense peak of $C_6H_3CN^{2+}$ at m/z = 50.5 is

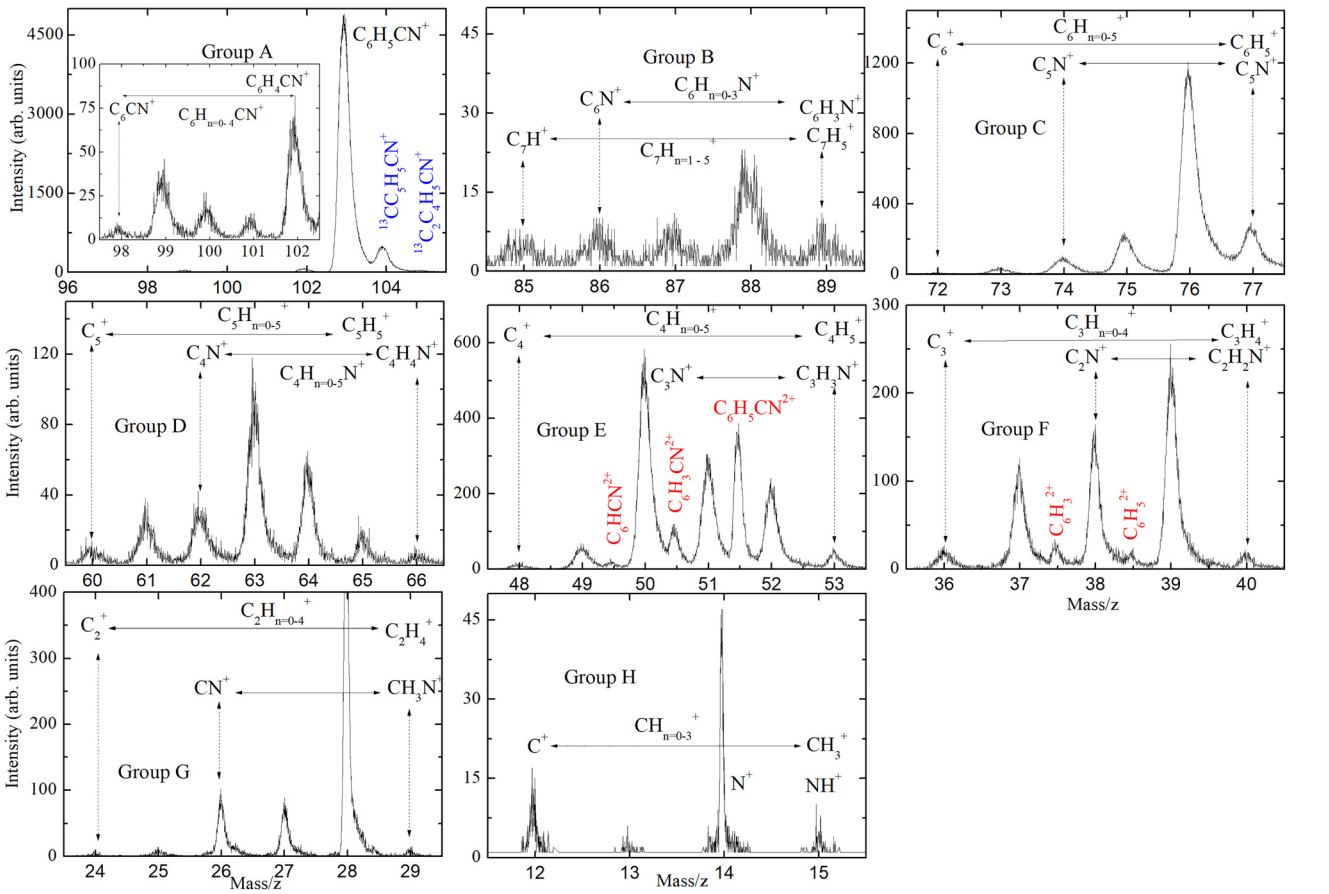

Fig. 2 Mass spectrum collected at 125 eV electron energy divided into 8 groups labelled A–H, with the indication of the species assigned to the mass/charge. Isotopes and doubly charged ions are indicated in blue and red, respectively.

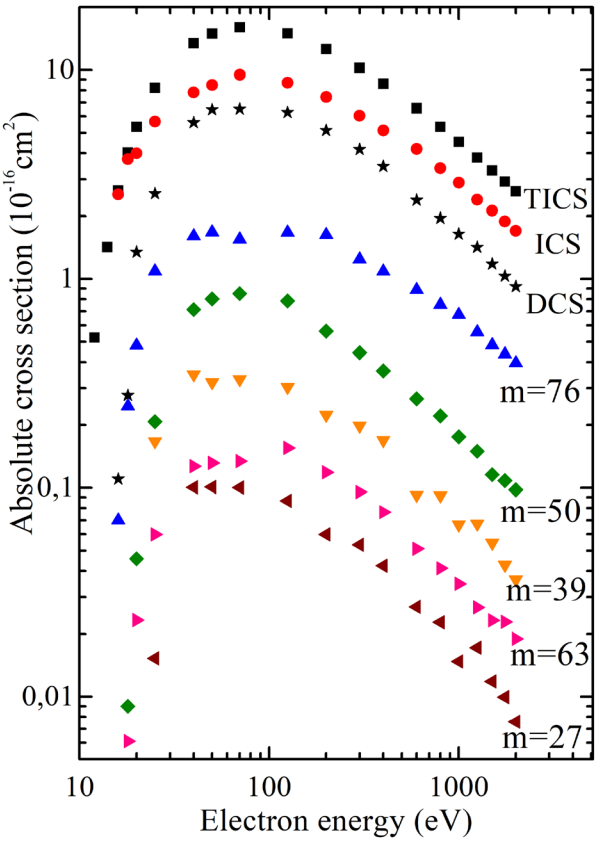

Fig. 3 Calculated total ionization cross sections (TICS)[53] and present measured cross sections: non-dissociative single ionization (ICS) and destruction DCS, which corresponds to the sum of all fragment cross sections and dissociative ionization cross sections of fragments with masses *m* (indicated to the 2000 eV electron energy), representative of the ionic groups A–G (see Fig. 2).

approximately 1/3 that of m/z = 51.5. The species C_6HCN^{2+} are very weak (see Fig. 2e) and were not quantified in the present work.

The low-energy isomers of $C_6H_5CN^{2+}$ and $C_6H_3CN^{2+}$ are presented in Fig. 5, first and second rows, respectively. The

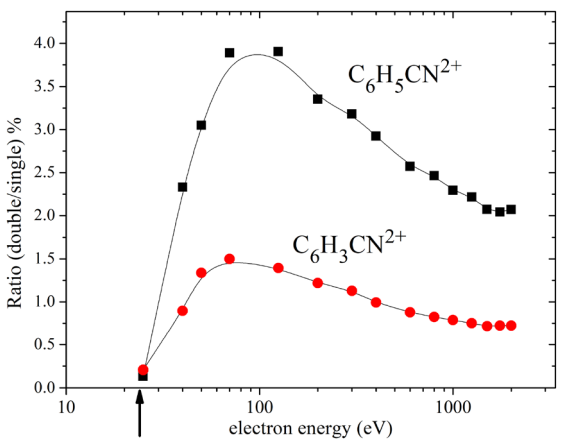

Fig. 4 Ratio of dications $C_6H_5CN^{2+}$ and $C_6H_3CN^{2+}$ relative to the parent ionized ion indicated in percentage.

$C_6H_5CN^{2+}$ GM can be formed by migration of hydrogen atoms from the aromatic ring to the CN group, forming $C_6H_4CNH^{2+}$ (para position, 5.1^{2+} in Fig. 5). The third structure (5.3^{2+}) in Fig. 5 is very similar, but the CNH group is present in the meta position. In the case of the second (5.2^{2+}) and fourth (5.4^{2+}) structures in Fig. 5, a linear chain connects the cyclopropenylium to the CNH group.

All isomers of $C_6H_3CN^{2+}$ present a cumulenic linear carbon chain, very similar to the cases of $C_5H_3N^+$, $C_6H_3N^{2+}$ and $C_7H_3N^{2+}$.[17,48,54] The global minimum candidate has the structure $CH_2C_5CNH^{2+}$ (3.1^{2+} in Fig. 5), which is a protonated isonitrile (which has the CNH group), similar to the structure $C_5H_3N^+$.[48] The second structure (3.2^{2+} in Fig. 5) is related to the GM but with the migration of a hydrogen atom to the second carbon atom (CHC_4CHCNH^{2+}). Migration was also observed for the $C_5H_3N^+$ system. The third structure (3.3^{2+} in Fig. 5) describes the $NH_2C_7H^{2+}$ molecule, and the fourth (3.4^{2+} in Fig. 5) presents a cyclopropenylium group, $C_3H_2C_3CNH^{2+}$, which is again similar to a low-energy isomer of $C_5H_3N^+$. Geometric parameters (bond lengths, angles, and charge distributions) of the GM candidates for doubly charged species are shown in Fig. S2–S11 in the SI.

4.2. Ionic species in the condensed phase

The ion emission is conducted by nonthermal processes, such as induced desorption by electronic transitions (DIET). The interatomic Auger decay prompts the creation of valence holes in the electronic band structure of the solid. The hole pairs remain localized for a short time (10 to 100 fs) but rapidly dissociate as a result of Coulomb repulsion, ejecting ions from the surface. Strong valence hole localization is expected in weakly physisorbed adsorbates; otherwise, rapid hole diffusion would quench Coulombic repulsion.[55]

Diverse intermolecular interactions occur at temperatures lower than 200 K[56] and induce the production of an extended mass range of hydrocarbons and nitrogen- and oxygen-containing species.[57–60] Large-mass charged ions have been suggested to be the signature of aerosol formation in Titan.[61–64]

The ion production depends on the phase and crystalline structure of the condensate. Time-of-flight mass spectra were recorded at two sample temperatures, one at 120 K, named "full multilayer", and another at 160 K, called "few-layer", to investigate the differences caused in the sample deposition and film formation. As the temperature increased, the diffusion process was triggered.

Fig. 6 illustrates the temperature-programmed desorption profile of ionized CN–Bz, showing three features, one starting at 130 to 160 K, the second from 160 to 190 K, and the last in the interval 190 to 220 K. This suggests that more than one crystalline structure can be formed through phase separation. They are present in the alpha and beta transition layers of CN–Bz condensates. Based on previous studies at low temperatures,[65,66] we suggest that physisorption took action in CN–Bz film formation, which aligns with evidence that chemisorption can only be observed at higher temperatures, above 280 K. CN–Bz exhibits two condensed phase transitions

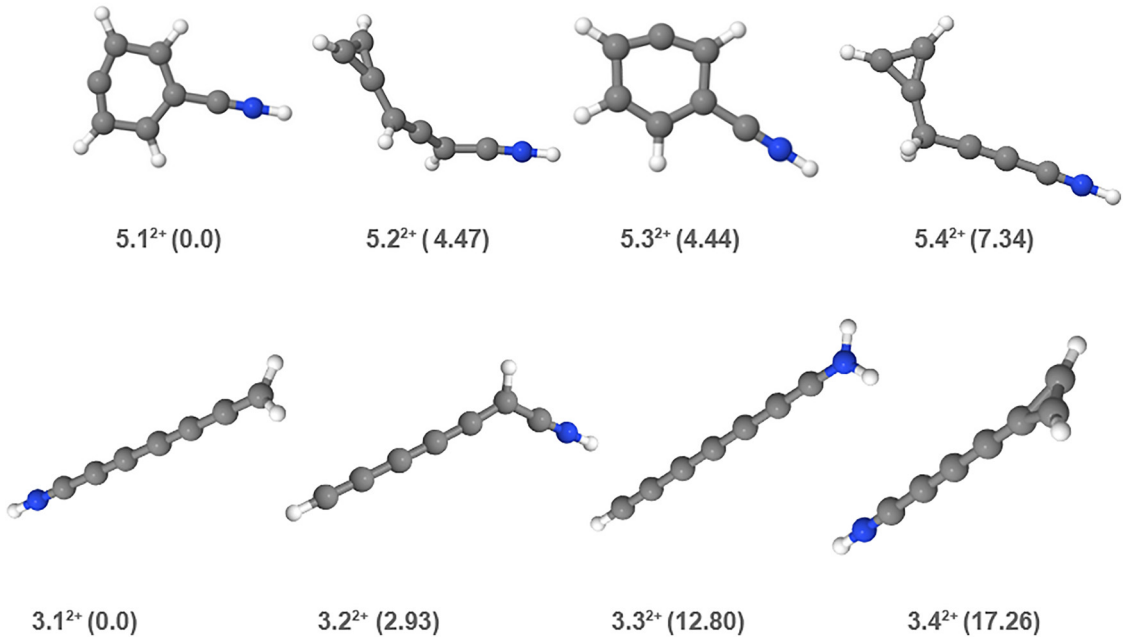

Fig. 5 Low-energy isomers of $C_6H_5CN^{2+}$ (m/z = 51.5) (top) and $C_6H_3CN^{2+}$ (m/z = 50.5) (bottom) obtained with the ABCluster software combined with DFT computations. Carbon atoms are gray, hydrogen atoms are white and nitrogen atoms are blue. The numbers in parentheses are the relative energies in kcal mol^{-1} obtained at the CCSD(T)/cc-pVTZ level of theory. Energy parameters and T1 diagnostics are shown in Tables S8 and S9 (SI).

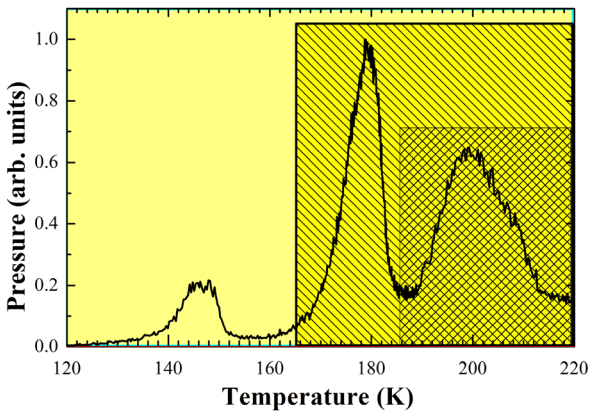

Fig. 6 Spectrum of temperature programmed desorption, with relative pressure as a function of temperature (in Kelvin).

around 188 K and 209 K,[66] changing the structure of the condensate. The findings corroborate the observations in the TPD spectrum. The features centered below 160 K and around 185 K formed the multilayer and few-layer structures, respectively, while the feature around 220 K is probably due to physisorption to the stainless steel substrate. Physisorption of CN–Bz on metal surfaces begins above 220 K.[65,66]

In addition, assuming that the desorption of the CN–Bz layer directly bonded to the metal substrate follows first-order kinetics and that the frequency factor is typically in the range[67] of 10^{13} s^{-1} to 10^{17} s^{-1}, we can apply Readhead's equation $E_d \approx RT_p\left[\ln\left(\frac{\nu_1 T_p}{\beta}\right)\right]$.[68,69] We estimate that the desorption energy of the TPD peak centered around 220 K is in the range of 62 to 82 kJ mol^{-1} under the present experimental conditions (heating rate: 0.1 K s^{-1}). This led us to infer that CN–Bz physically adsorbs to the metal substrate, since chemisorption is expected to exhibit higher desorption energies, generally above 90 kJ mol^{-1}.[69]

Increasing the temperature of the substrate through resistive heating from 120 K to 170 K and then cooling it back to 120 K improves mobility in the crystalline CN–Bz structure, reorienting (tilting) or disordering the molecules. The warming process induces more contributions of weaker forces in comparison with chemical bonds, such as van der Waals interactions between the chains. The enhanced mobility leads to the formation of more molecular aggregates in the crystal structure, called a "few-layer".

Fig. 7 shows the ions desorbed from the (a) multilayer and (b) few-layer CN–Bz films and (c) the changes induced by the increase in temperature from 120 to 170 K. The few-layer (FL) structure showed a higher yield of hydrogenated molecules. For example, cyanide ion (HCN^+, m/z = 27) has a much higher yield than methanimine cation (CH_3N^+, m/z = 29), under multilayer (ML) conditions. However, for the FL structure, we observe the opposite: there is a higher yield of m/z = 29 compared to m/z = 27. These differences are more evident in Fig. 7(c), where "positive" yields indicate a higher production of mass/charge in the FL structure compared to the ML structure. Negative yields indicate a higher production of mass/charge in the ML structure. Although a negative yield is observed in the mass regions m/z = 39–43, there is an inversion in the production of C_2HN^+ or $C_3H_3^+$ (cyclopropenium ion) in the FL and ML films. The higher number of hydrogenated ionic species in the FL range occurs because the increase in temperature promotes a

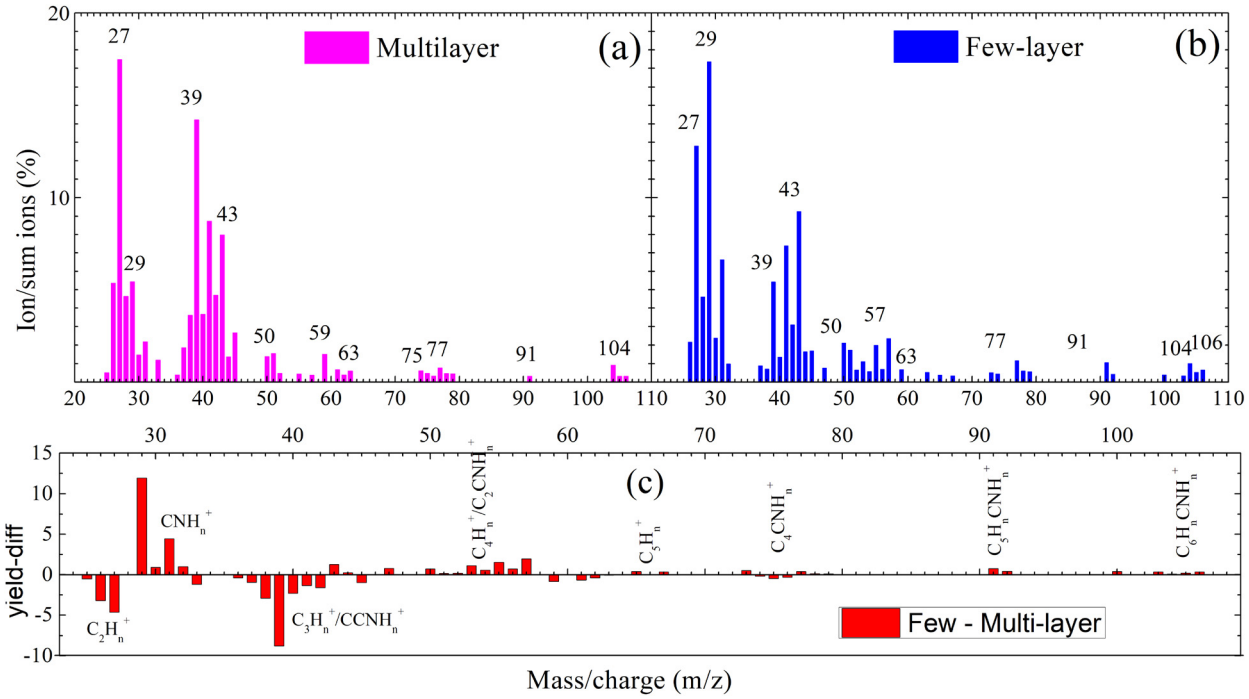

Fig. 7 Condensed benzonitrile – (a) multilayer film, (b) few-layer sample, and (c) comparison of multilayer and few-layer structures: subtraction of the few-layer yield from the multilayer one.

phase change.[65,66] For the parent molecule (m/z = 103), only its hydrogenated forms were observed. The species of m/z = 106, which corresponds to the fragment after triple hydrogenation, was detected mainly in the FL range.

5. Comparison of ionic species in the gas and condensed phase

The ionic fragments in the gaseous phase were mostly similar to those in the condensed phase according to the spectral results. The single- and multiple-hydrogen losses present in the gas phase are almost absent in the condensed phase. In contrast, cluster-ion formation is absent in gas-phase experiments in the single-collision regime, but is expected in high-density environments, such as in condensed samples and in supersonic jet expansion under vacuum. Ionic fragments and clusters attached to radicals are formed at the surface, gain enough energy to surmount the surface potential, and can leave the surface. In gas phase measurements, the metastable dicationic species were detected, while on surfaces, efficient neutralization processes make their detection mostly inaccessible.

The fragmentation mechanisms change the intensities of the cations, as shown in Fig. 8, which illustrates a comparison

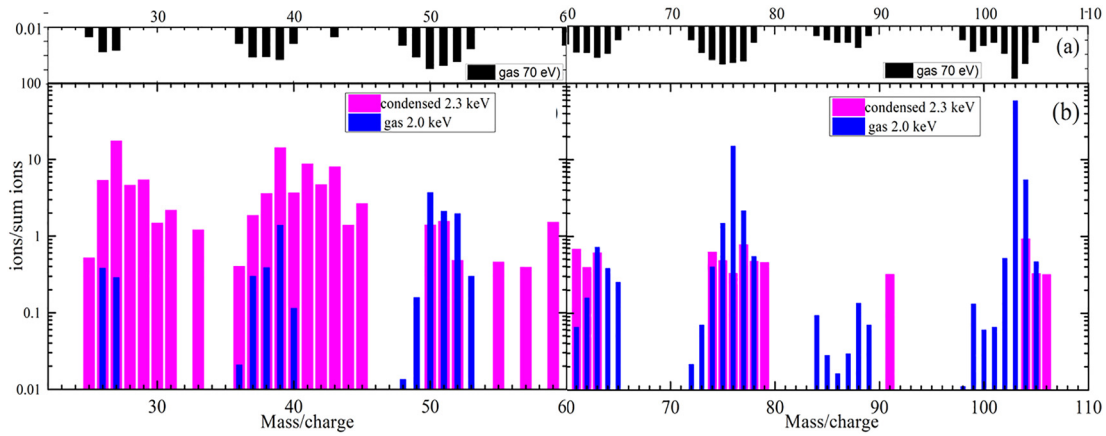

Fig. 8 Yields of cations with mass/charge from m/z = 20–110 produced in the gas phase and desorbed in the condensed phase (multilayer film) indicated in blue and magenta, respectively. At the top, to better highlight the differences, yields of cations formed in the gas phase by 70 eV electrons are included.

between the yields obtained with 2300 eV electrons in condensed CN–Bz in relation to those with 2000 eV electrons from the gas phase measurements. The yields up to protonated CN–Bz and ionized CN–Bz are structured in groups. The lighter ions show an enhanced multiple attachment of hydrogen atoms in comparison with the heavier ones. Single hydrogenation is the rule in these cases. The role of intermolecular interactions for condensed hydrogen-bonded molecules has been previously studied and suggests that strong bond energies favor proton-transfer reactions or dimer formation, rather than simple molecular dissociation.[70,71]

5.1. Global minimum structures of aggregates (m/z = 104–106)

The candidates for the global minimum structure for m/z = 104 are shown in Fig. 9. The lowest energy isomer is protonated benzonitrile forming $C_6H_5CNH^+$ (6.1^+ in Fig. 9). The second (6.2^+) and third (6.3^+) structures in Fig. 9 have an NH group in the six-membered ring, similar to some low-energy isomers of aniline polycations[72] but with C_2H as the lateral group. The fourth structure (6.4^+) is a fused bicyclic heterocycle with two five-membered rings, respectively. In the case of m/z = 105, $C_6H_5CHNH^+$ (Fig. 9), the four lowest energy isomers are very close in energy, exhibiting a five-membered ring, which are also fused bicyclic heterocycles. For m/z = 106, $C_6H_5CHNH_2^+$ (Fig. 9), the GM candidate is the α-aminobenzyl (8.1^+), in agreement with the previous result.[73,74] The second structure (8.2^+ in Fig. 9) was not proposed in previous work and is composed of a cyclic C_5H_4 NH bonded to a $CHCH_2$ group that forms $C_5H_4NHCHCH_2^+$. The third (8.3^+) and fourth (8.4^+) structures are four- and six-membered rings.

6. Astrophysical implications – benzonitrile in the Titan atmosphere

Magnetosphere electrons are considered the main radiation source of the night-side ionosphere of Titan (at least for altitudes above 1000 km),[13,14] while photoelectrons predominate the day-side ionosphere.

The experimental data collected by Cassini/Huygens flybys[61,75–77] and the previous Voyager mission have revealed charged ions in the upper atmosphere of Titan.[59,62,63,78–83] Cassini ion and neutral mass spectrometer (INMS) has detected organic species in the mass range of 1 to 100 Daltons at Titan altitudes of around 1000 km.[63,83,84] Similarly, the data collected by the Cassini ion beam and electron spectrometer (IBS and ELS) have indicated the presence of charged ions of higher mass than those detected by the ion and neutral mass spectrometer (INMS)[63]

The mean half-life of CN–Bz under electron impact was estimated within the present electron energy range combined with the electron fluxes collected by the plasma-electron spectrometers CAPS of the Cassini spacecraft on the night side of Titan during flybys T5 and T57, at the lowest (990 km) and highest (2700 km) altitudes, respectively,[85] during the T40 flyby on the day side (~1100 km),[86] and by Voyager from 630 to 1250 km[87] (see Fig. S17, SI).

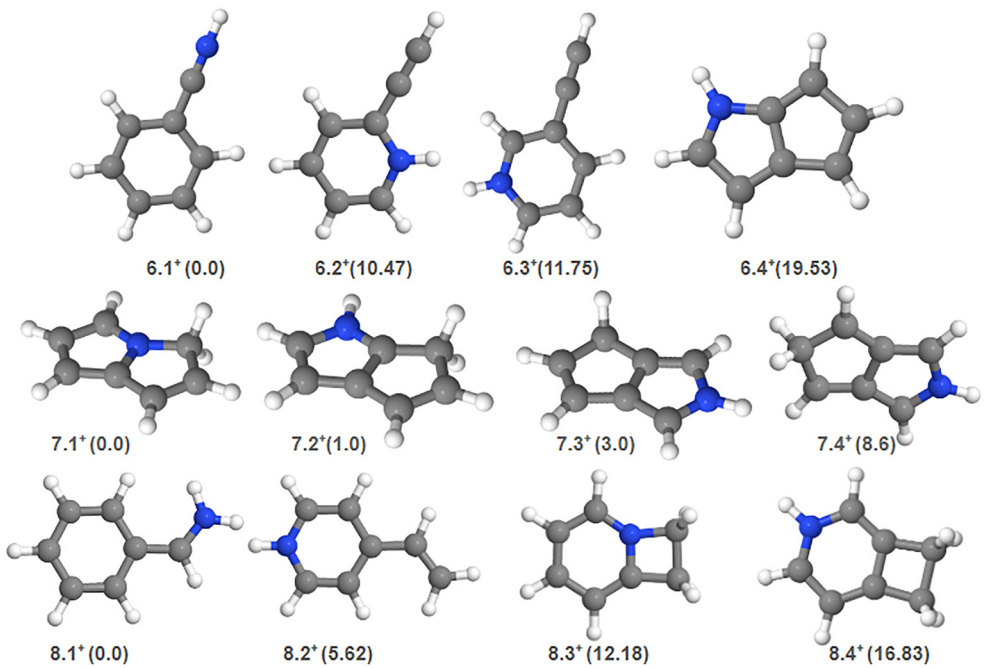

Fig. 9 Low-energy isomers of $C_6H_5CNH^+$ (m/z = 104) (top), $C_6H_5CHNH^+$ (m/z = 105) (middle) and $C_6H_5CHNH_2^+$ (m/z = 106) (bottom), obtained with the ABCluster software combined with DFT computations. Carbon atoms are gray, hydrogen atoms are white and nitrogen atoms are blue. The numbers in parentheses are the relative energies in kcal mol^{-1} obtained at the CCSD(T)/cc-pVTZ level of theory. Energy parameters and T1 diagnostics for CCSD(T) are shown in Tables S10–S12 (SI). For details about CASSCF/NEVPT2/def2-TZVP energies and active space orbitals, see Table S11 and Fig. S12–S15 in the SI.

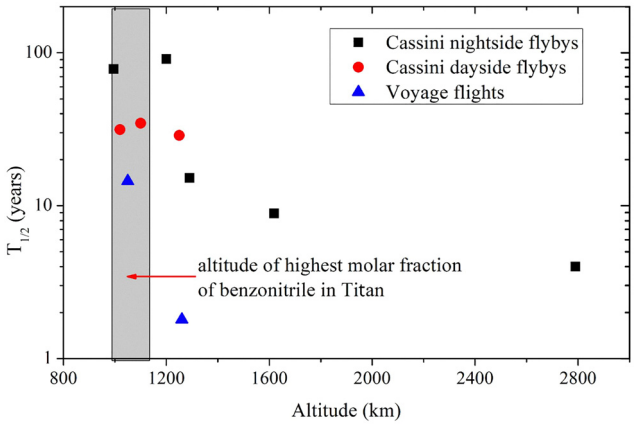

Fig. 10 Half-life (Earth years) as a function of the altitude (km). Black squares: half-life considering fluxes of magnetosphere electrons measured by Cassini flybys T5 and T57 at the night-side face of Titan; red circles: half-life considering fluxes of secondary electrons from solar wind measured by Cassini flybys T40 at the day-side face of Titan; and blue triangles: half-life calculation with fluxes of electrons collected by Voyager flybys.

Magnetosphere electrons determine a half-life of CN–Bz on the same order of magnitude compared to secondary electrons (see Fig. 10). The destruction rate as a function of the electron impact energy is shown in Fig. S18 (SI) for the electron fluxes measured by the flyby T40 on the night side face of Titan at an altitude of 1020 km. In the altitude range (1000–1150 km) with the highest molar fraction of CN–Bz, Fig. 10 shows a half-life of ~40 and 90 Earth years on the day and night side of Titan, respectively. It should be noted that the nominal models estimate the chemical and dynamical lifetimes to be 0.73 years for benzene, 13.2 years for HCN, and 27.7 years for CH_3CN for altitudes from 200 to 1200 km (see Discussion in the SI).

Antagonist conditions apply to molecular formation and stability at low altitudes. The molecular density at high altitudes acts as a shield from radiation, reducing the particle fluxes and protecting the molecular surroundings at low altitudes. However, the Saturn magnetosphere can act on the incident impact electron energy, accelerating them towards the surface.

The Huygens gas chromatograph mass spectrograph measured the composition of the atmosphere below 146 km altitude to the surface ~7 km, including up to 140 Daltons.[58,81] The measurements did not show the presence of many heavy molecules, but there is an indication of the mass of CN–Bz. Heavy hydrocarbons and nitriles avoid condensation at low temperatures in the lower stratosphere (below 200 km) and troposphere,[32,88] but there is a probability of detecting some of them, which can have precipitated from the upper atmosphere.[58,81]

Experiments simulating the production of Titan's haze using an aerosol mass spectrometer examined the chemical structure of haze particles under different conditions.[89] Voyager spacecraft observed tholins[90] at ~500 km, while Cassini only observed them at lower altitudes, ~380 km. In another haze experiment, atmospheric chemistry was simulated similar to that found in regions where aerosols are present (~150 K).[91] Electrons and ions were detected above 900 km and are probably the seeds of haze aerosols observed at altitudes ~500 km[32,92] to 100 km.[93]

The predicted CN–Bz production on the night and day-side face is weak, as CN is significantly consumed by reaction with CH_4.[94] The mole fraction of CN–Bz was between 1×10^{-9} at 1000 km and 1×10^{-14} at 350 km.[94] Through direct bimolecular reactions between CN radicals and benzene, CN–Bz formation was estimated with a reaction rate coefficient of $(4.0) \times 10^{-10}$ cm^3 molecule^{-1} s^{-1}.[94] This estimate is in agreement with the experimental one of $(3.9) \times 10^{-10}$ cm^3 molecule^{-1} s^{-1} at the relevant Titan temperature of 105 K.[7] Although the reaction channel "CN + benzene" is barrierless and the radical C_6H_6 CN can be produced, only 2% dissociate to form cyanobenzene.[7] The conditions indicate that the presence of CN–Bz$^+$ may be too small to be detected in the Titan atmosphere despite its strong dipole moment (4.71 D),[95] which had allowed detection in the Taurus molecular cloud (TMC-1).[5]

CN–Bz has been detected in tholin pyrolyzates obtained as a minor component in spark discharge synthesis experiments.[90,96] The temperature allows for the nucleation of ice aerosols or the condensation of ice layers on the surfaces. The species are predicted to survive for months to years in the lower Titan atmosphere. Long descents can allow chemistry to unfold on the surface and within the bulk of haze aerosols.

7. Conclusion

We studied the impact of radiation sources, such as electrons, on the CN–Bz molecule. In the condensed phase, the experiments show that molecular fragments react with others in association reactions, whereas in the gas phase, pure ionization dominates. Even then, in the gas phase, the sum of all ion fragments contributes on average with ~1/3 of the total ionization cross section. The present setup is not able to distinguish between isomers with the same chemical formula, but the calculation may infer the species. The study suggests that benzonitrile species should have a rather low lifetime in the Titan atmosphere because of the order of absolute ionization cross-section values and high electron fluxes. The molecules to be explored are the species that result from condensation and sedimentation to the surface. The results suggest that laboratory experiments can be used in addition to observational data to predict both the presence and the possible detection of molecules, such as gaseous and condensed CN–Bz, that have not yet been detected.

Conflicts of interest

There are no conflicts to declare.

Data availability

The data supporting this article have been included as part of the supplementary information (SI). Supplementary

information: cations in Titan and dications in solar atmospheres. Five, six and larger aromatic cyano rings. Admission spectrum. Absolute cross sections. Vibrational frequencies for isomers. Geometric parameters. Energy parameters. CASSCF Active Space for m/z 105 G.M. candidates. Destruction rate for the T40 flyby.

Additional data or clarifications are available from the authors upon reasonable request.

Acknowledgements

The authors thank the PTB for the experimental support. The authors acknowledge the Conselho Nacional de Desenvolvimento Científico e Tecnológico (CNPq), Coordenacao de Aperfeicoamento Pessoal de Nivel Superior (CAPES) and Fundação de Amparo à Pesquisa do Estado do Rio de Janeiro (FAPERJ). The National Laboratory for Scientific Computing (LNCC/MCTI, Brazil) has provided HPC resources of the SDumont supercomputer, which have contributed to the research results (**https://sdumont.lncc.br**), and the DIRAC computer cluster from Rede de Teoria, Modelagem, e Simulação de Materiais para Nanotecnologia. Also, RRO thanks FAPERJ for financial support with grant number E-26/200.249/2023.

References

1 K. L. Kelvin Lee, P. B. Changala, R. A. Loomis, A. M. Burkhardt, C. Xue, M. A. Cordiner, S. B. Charnley, M. C. McCarthy and B. A. McGuire, *Astrophys. J., Lett.*, 2021, **910**, L2.
2 M. L. Sita, P. B. Changala, C. Xue, A. M. Burkhardt, C. N. Shingledecker, K. L. Kelvin Lee, R. A. Loomis, E. Momjian, M. A. Siebert, D. Gupta, E. Herbst, A. J. Remijan, M. C. McCarthy, I. R. Cooke and B. A. McGuire, *Astrophys. J., Lett.*, 2022, **938**, L12.
3 J. Cernicharo, C. Cabezas, R. Fuentetaja, M. Agendez, B. Tercero, J. Janeiro, M. Juanes, R. I. Kaiser, Y. Endo, A. L. Steber, D. Perez, C. Perez, A. Lesarri, N. Marcelino and P. de Vicente, *Astron. Astrophys.*, 2024, **690**, L13.
4 G. Wenzel, I. R. Cooke, P. B. Changala, E. A. Bergin, S. Zhang, A. M. Burkhardt, A. N. Byrne, S. B. Charnley, M. A. Cordiner, M. Duffy, Z. T. P. Fried, H. Gupta, M. S. Holdren, A. Lipnicky, R. A. Loomis, H. T. Shay, C. N. Shingledecker, M. A. Siebert, D. A. Stewart, R. H. J. Willis, C. Xue, A. J. Remijan, A. E. Wendlandt, M. C. McCarthy and B. A. McGuire, *Science*, 2024, **0**, eadq6391.
5 B. A. McGuire, A. M. Burkhardt, S. Kalenskii, C. N. Shingledecker, A. J. Remijan, E. Herbst and M. C. McCarthy, *Science*, 2018, **359**, 202–205.
6 B. A. McGuire, R. A. Loomis, A. M. Burkhardt, K. L. K. Lee, C. N. Shingledecker, S. B. Charnley, I. R. Cooke, M. A. Cordiner, E. Herbst, S. Kalenskii, M. A. Siebert, E. R. Willis, C. Xue, A. J. Remijan and M. C. McCarthy, *Science*, 2021, **371**, 1265–1269.
7 A. J. Trevitt, F. Goulay, C. A. Taatjes, D. L. Osborn and S. R. Leone, *J. Phys. Chem. A*, 2010, **114**, 1749–1755.
8 D. E. Woon, *Chem. Phys.*, 2006, **331**, 67–76.
9 N. Balucani, O. Asvany, A. H. H. Chang, S. H. Lin, Y. T. Lee, R. I. Kaiser, H. F. Bettinger, P. V. R. Schleyer and H. F. Schaefer, *J. Chem. Phys.*, 1999, **111**, 7457–7471.
10 K. L. K. Lee, B. A. McGuire and M. C. McCarthy, *Phys. Chem. Chem. Phys.*, 2019, **21**, 2946–2956.
11 V. Vuitton, R. V. Yelle and J. Cui, *J. Geophys. Res.*, 2008, **113**, E05007.
12 C. Freissinet, D. P. Glavin, P. D. Archer, S. Teinturier, A. Buch, C. Szopa, J. M. T. Lewis, A. J. Williams, R. Navarro-Gonzalez, J. P. Dworkin, H. B. Franz, M. Millan, J. L. Eigenbrode, R. E. Summons, C. H. House, R. H. Williams, A. Steele, O. McIntosh, F. Gómez, B. Prats, C. A. Malespin and P. R. Mahaffy, *Proc. Natl. Acad. Sci. U. S. A.*, 2025, **122**, e2420580122.
13 F. Raulin, *Space Sci. Rev.*, 2002, **104**, 377–394.
14 F. Raulin, C. Brassé, O. Poch and P. Coll, *Chem. Soc. Rev.*, 2012, **41**, 5380–5393.
15 A. Marten, T. Hidayat, Y. Biraud and R. Moreno, *Icarus*, 2002, **158**, 532–544.
16 J. Jasik, D. Gerlich and J. Roithová, *J. Am. Chem. Soc.*, 2014, **136**, 2960–2962.
17 W. Wolff, A. Perlin, R. R. Oliveira, F. Fantuzzi, L. H. Coutinho, F. A. de Ribeiro and G. Hilgers, *J. Phys. Chem. A*, 2020, **124**, 9261–9271.
18 D. Mathur, L. H. Andersen, P. Hvelplund, D. Kella and C. P. Safvan, *J. Phys. B: At., Mol. Opt. Phys.*, 1995, **28**, 3415.
19 D. Mathur, L. Andersen, P. Hvelplund, D. Kella and C. Safvan, *J. Phys. B: At., Mol. Opt. Phys.*, 1999, **28**, 3415.
20 J. Lilensten, O. Witasse, C. Simon Wedlund, H. Dossmann, O. Dutuit, R. Thissen and C. Alcaraz, *Geophys. Res. Lett.*, 2005, **32**, 781–797.
21 J. Lilensten, C. S. Wedlund, M. Barthélémy, R. Thissen, D. Ehrenreich, G. Gronoff and O. Witasse, *Icarus*, 2013, **222**, 169–187.
22 M. Dobrijevic, E. Hébrard, J. Loison and K. Hickson, *Icarus*, 2014, **228**, 324–346.
23 T. Matsubara, *Bull. Chem. Soc. Jpn.*, 2024, **97**, uoae047.
24 D. B. Rap, A. Simon, K. Steenbakkers, J. G. Schrauwen, B. Redlich and S. Brünken, *Faraday Discuss.*, 2023, **245**, 221–244.
25 D. Bou Debes, M. Mendes, R. Rodrigues, J. Ameixa, L. M. Cornetta, F. Ferreira da Silva and S. Eden, *Astron. Astrophys.*, 2025, **693**, A304.
26 M. A. Baldwin, *Org. Mass Spectrom*, 1979, **14**, 601–605.
27 D. B. Rap, J. G. M. Schrauwen, B. Redlich and S. Brünken, *Phys. Chem. Chem. Phys.*, 2024, **26**, 7296–7307.
28 B. Rajasekhar, V. Dharmarpu, A. K. Das, A. Shastri, A. Veeraiah and S. Krishnakumar, *J. Quant. Spectrosc. Radiat. Transfer*, 2022, **283**, 108159.
29 H. M. Rosenstock, R. P. Stockbauer and C. Albert, *J. Chim. Phys.*, 1980, **77**, 745–750.
30 F. C. Daly, T. E. Douglas-Walker, J. Palotas, C. S. Anstoter, A. Zheng and E. K. Campbell, *J. Chem. Phys.*, 2024, **161**, 074305.
31 W. B. Martin and R. M. O'Malley, *Int. J. Mass Spectrom. Ion Processes*, 1984, **59**, 277–294.

32 E. Wilson and S. Atreya, *Planet. Space Sci.*, 2003, **51**, 1017–1033.
33 E. Hébrard, M. Dobrijevic, Y. Bénilan and F. Raulin, *J. Photochem. Photobiol., C*, 2006, **7**, 211–230.
34 N. Carrasco, S. Plessis, M. Dobrijevic and P. Pernot, *Int. J. Chem. Kinet.*, 2008, **40**, 699–709.
35 P. Lavvas, R. V. Yelle and V. Vuitton, *Icarus*, 2009, **201**, 626–633.
36 V. A. Krasnopolsky, *Planet. Space Sci.*, 2010, **58**, 1507–1515.
37 V. Esposito, S. Alessandrini, D. Dubois and R. Fortenberry, *Planet. Sci. J.*, 2025, **6**, 1–14, DOI: **10.3847/PSJ/adcf17**.
38 M. Ruaud, V. Wakelam and F. Hersant, *Mon. Not. R. Astron. Soc.*, 2016, **459**, 3756–3767.
39 K. L. K. Lee, B. A. McGuire and M. C. McCarthy, *Phys. Chem. Chem. Phys.*, 2019, **21**, 2946–2956.
40 A. Taghipour, J. A. Ramirez, R. J. Brown and T. J. Rainey, *Renewable Sustainable Energy Rev.*, 2019, **115**, 109355.
41 W. Wolff, A. M. R. Giraldi, J. H. C. Basilio, F. de, A. Ribeiro, A. N. Oliveira and R. R. Oliveira, *J. Phys. Chem. A*, 2025, **129**(15), 3389–3400.
42 J. Zhang and M. Dolg, *Phys. Chem. Chem. Phys.*, 2015, **17**, 24173–24181.
43 J. Zhang and M. Dolg, *Phys. Chem. Chem. Phys.*, 2016, **18**, 3003–3010.
44 C. Bannwarth, S. Ehlert and S. Grimme, *J. Chem. Theory Comput.*, 2019, **15**, 1652–1671.
45 V. S. Thimmakondu, A. Sinjari, D. Inostroza, P. Vairaprakash, K. Thirumoorthy, S. Roy, A. Anoop and W. Tiznado, *Phys. Chem. Chem. Phys.*, 2022, **24**, 11680–11686.
46 F. Neese, F. Wennmohs, U. Becker and C. Riplinger, *J. Chem. Phys.*, 2020, **152**, 224108.
47 F. Neese, *WIREs Comput. Mol. Sci.*, 2022, **12**, e1606.
48 A. L. Perlin, W. Wolff and R. R. Oliveira, *J. Phys. Chem. A*, 2023, **127**, 2481–2488.
49 J. C. Santos, F. Fantuzzi, H. M. Quitian Lara, Y. Martins Franco, K. Menndez Delmestre, H. M. Boechat Roberty and R. R. Oliveira, *Mon. Not. R. Astron. Soc.*, 2022, **512**, 4669–4682.
50 T. J. Lee and P. R. Taylor, *Int. J. Quantum Chem.*, 2009, **36**, 199–207.
51 K. K. Irikura, *J. Chem. Phys.*, 2016, **145**, 224102.
52 K. K. Irikura, *J. Res. Natl. Inst. Stan.*, 2017, **122**, 1–67, DOI: **10.6028/jres.122.028**.
53 D. Gupta, H. Choi, S. Singh, P. Modak, B. Antony, D.-C. Kwon, M.-Y. Song and J.-S. Yoon, *J. Chem. Phys.*, 2019, **150**, 064313.
54 T. Monfredini, F. Fantuzzi, M. A. C. Nascimento, W. Wolff and H. M. Boechat-Roberty, *Astrophys. J.*, 2016, **821**, 4.
55 R. Souda, *Surf. Sci. Lett.*, 2002, **506**, L275–L281.
56 M. Fulchignoni, F. Ferri, F. Angrilli, A. J. Ball, A. Bar-Nun, M. A. Barucci, C. Bettanini, G. Bianchini, W. Borucki, G. Colombatti, M. Coradini, A. Coustenis, S. Debei, P. Falkner, G. Fanti, E. Flamini, V. Gaborit, R. Grard, M. Hamelin, A. M. Harri, B. Hathi, I. Jernej, M. R. Leese, A. Lehto, P. F. Lion Stoppato, J. J. Lopez-Moreno, T. Mäkinen, J. A. M. McDonnell, C. P. McKay, G. Molina-Cuberos, F. M. Neubauer, V. Pirronello, R. Rodrigo, B. Saggin, K. Schwingenschuh, A. Seiff, F. SimÃµes, H. Svedhem, T. Tokano, M. C. Towner, R. Trautner, P. Withers and J. C. Zarnecki, *Nature*, 2005, **438**, 785–791.
57 F. M. Flasar, R. K. Achterberg, B. J. Conrath, P. J. Gierasch, V. G. Kunde, C. A. Nixon, G. L. Bjoraker, D. E. Jennings, P. N. Romani, A. A. Simon-Miller, B. Bezard, A. Coustenis, P. G. J. Irwin, N. A. Teanby, J. Brasunas, J. C. Pearl, M. E. Segura, R. C. Carlson, A. Mamoutkine, P. J. Schinder, A. Barucci, R. Courtin, T. Fouchet, D. Gautier, E. Lellouch, A. Marten, R. Prangee, S. Vinatier, D. F. Strobel, S. B. Calcutt, P. L. Read, F. W. Taylor, N. Bowles, R. E. Samuelson, G. S. Orton, L. J. Spilker, T. C. Owen, J. R. Spencer, M. R. Showalter, C. Ferrari, M. M. Abbas, F. Raulin, S. Edgington, P. Ade and E. H. Wishnow, *Science*, 2005, **308**, 975–978.
58 H. B. Niemann, S. K. Atreya, J. E. Demick, D. Gautier, J. A. Haberman, D. N. Harpold, W. T. Kasprzak, J. I. Lunine, T. C. Owen and F. Raulin, *J. Geophys. Res.*, 2010, **115**, E12006.
59 N. A. Teanby, M. Sylvestre, J. Sharkey, C. A. Nixon, S. Vinatier and P. G. J. Irwin, *Geophys. Res. Lett.*, 2019, **46**, 3079–3089.
60 J. Cui, M. Galand, R. V. Yelle, V. Vuitton, J.-E. Wahlund, P. P. Lavvas, I. C. F. Müller-Wodarg, T. E. Cravens, W. T. Kasprzak and J. H. Waite, *J. Geophys. Res.*, 2009, **114**, A06310.
61 P. Lavvas, R. V. Yelle, T. Koskinen, A. Bazin, V. Vuitton, E. Vigren, M. Galand, A. Wellbrock, A. J. Coates, J.-E. Wahlund, F. J. Crary and D. Snowden, *Proc. Natl. Acad. Sci. U. S. A.*, 2013, **110**, 2729–2734.
62 A. J. Coates, F. J. Crary, G. R. Lewis, D. T. Young, J. H. Waite Jr. and E. C. Sittler Jr., *Geophys. Res. Lett.*, 2007, **34**, L22103.
63 J. H. Waite, D. T. Young, T. E. Cravens, A. J. Coates, F. J. Crary, B. Magee and J. Westlake, *Science*, 2007, **316**, 870–875.
64 J.-E. Wahlund, M. Galand, I. Müller-Wodarg, J. Cui, R. Yelle, F. Crary, K. Mandt, B. Magee, J. Waite, D. Young, A. Coates, P. Garnier, K. Ågren, M. André, A. Eriksson, T. Cravens, V. Vuitton, D. Gurnett and W. Kurth, *Planet. Space Sci.*, 2009, **57**, 1857–1865.
65 F. Tao, Z. H. Wang and G. Q. Xu, *J. Phys. Chem. B*, 2002, **106**, 3557–3563.
66 T. Solomun, K. Christmann and H. Baumgaertel, *J. Phys. Chem.*, 1989, **93**, 7199–7208.
67 M. Schmid, G. S. Parkinson and U. Diebold, *ACS Phys. Chem. Au*, 2023, 44–62.
68 P. A. Redhead, *Vacuum*, 1962, 203–211.
69 D. P. Woodruff and T. A. Delchar, *Cambridge solid state science series: Modern techniques of surface science*, Cambridge University Press, Cambridge, England, 2nd edn, 2010.
70 F. d A. Ribeiro, G. C. Almeida, Y. Garcia-Basabe, W. Wolff, H. M. Boechat-Roberty and M. L. M. Rocco, *Phys. Chem. Chem. Phys.*, 2015, **17**, 27473–27480.
71 H. Cerqueira, J. Santos, F. Fantuzzi, F. Ribeiro, M. Rocco, R. Oliveira and A. Rocha, *J. Phys. Chem. A*, 2020, **124**, 6845–6855.

72 G. L. Gutsev, H. A. López Peña, S. L. McPherson, D. A. Boateng, B. R. Ramachandran, L. G. Gutsev and K. M. Tibbetts, *J. Phys. Chem. A*, 2020, **124**, 3120–3134.
73 E. T. M. Selim, M. A. Rabbih and M. A. Fahmey, *Org. Mass Spectrom.*, 1992, **27**, 919–923.
74 G. Bouchoux, J. D. Winter, R. Flammang and P. Gerbaux, *J. Phys. Chem. A*, 2010, **114**, 7408–7416.
75 R. Brown, J. Lebreton and J. Waite, *Titan from Cassini–Huygens*, Springer Netherlands, 2014.
76 V. Vuitton, R. Yelle and M. McEwan, *Icarus*, 2007, **191**, 722–742.
77 C. A. Nixon, *ACS Earth Space Chem.*, 2024, **8**, 406–456.
78 R. Hartle, E. Sittler, F. Neubauer, R. Johnson, H. Smith, F. Crary, D. McComas, D. Young, A. Coates, D. Simpson, S. Bolton, D. Reisenfeld, K. Szego, J. Berthelier, A. Rymer, J. Vilppola, J. Steinberg and N. Andre, *Planet. Space Sci.*, 2006, **54**, 1211–1224.
79 R. V. Yelle, N. Borggren, V. de la Haye, W. Kasprzak, H. Niemann, I. Müller-Wodarg and J. Waite, *Icarus*, 2006, **182**, 567–576.
80 S. Vinatier, B. Bézard, S. Lebonnois, N. A. Teanby, R. K. Achterberg, N. Gorius, A. Mamoutkine, E. Guandique, A. Jolly, D. E. Jennings and F. M. Flasar, *Icarus*, 2015, **250**, 95–115.
81 H. B. Niemann, S. K. Atreya, S. J. Bauer, G. R. Carignan, J. E. Demick, R. L. Frost, D. Gautier, J. A. Haberman, D. N. Harpold, D. M. Hunten, G. Israel, J. I. Lunine, W. T. Kasprzak, T. C. Owen, M. Paulkovich, F. Raulin, E. Raaen and S. H. Way, *Nature*, 2005, **438**, 779–784.
82 J. W. Barnes, J. M. Soderblom, R. H. Brown, B. J. Buratti, C. Sotin, K. H. Baines, R. N. Clark, R. Jaumann, T. B. McCord, R. Nelson, S. Le Mouélic, S. Rodriguez, C. Griffith, P. Penteado, F. Tosi, K. M. Pitman, L. Soderblom, K. Stephan, P. Hayne, G. Vixie, J.-P. Bibring, G. Bellucci, F. Capaccioni, P. Cerroni, A. Coradini, D. P. Cruikshank, P. Drossart, V. Formisano, Y. Langevin, D. L. Matson, P. D. Nicholson and B. Sicardy, *Planet. Space Sci.*, 2009, **57**, 1950–1962.
83 J. H. Waite, W. S. Lewis, W. T. Kasprzak, V. G. Anicich, B. P. Block, T. E. Cravens, G. G. Fletcher, W.-H. Ip, J. G. Luhmann, R. L. Mcnutt, H. B. Niemann, J. K. Parejko, J. E. Richards, R. L. Thorpe, E. M. Walter and R. V. Yelle, *Space Sci. Rev.*, 2004, **114**, 113–231.
84 T. Cravens, I. Robertson, J. Waite, R. Yelle, V. Vuitton, A. Coates, J.-E. Wahlund, K. Agren, M. Richard, V. De La Haye, A. Wellbrock and F. Neubauer, *Icarus*, 2009, **199**, 174–188.
85 M. S. Richard, T. E. Cravens, C. Wylie, D. Webb, Q. Chediak, R. Perryman, K. Mandt, J. Westlake, J. H. Waite Jr., I. Robertson, B. A. Magee and N. J. T. Edberg, *J. Geophys. Res.*, 2015, **120**, 1264–1280.
86 P. Lavvas, M. Galand, R. Yelle, A. Heays, B. Lewis, G. Lewis and A. Coates, *Icarus*, 2011, **213**, 233–251.
87 M. Galand, J. Lilensten, D. Toublanc and S. Maurice, *Icarus*, 1999, **140**, 92–105.
88 E. H. Wilson and S. K. Atreya, *J. Geophys. Res.*, 2004, **109**, E06002.
89 M. G. Trainer, A. A. Pavlov, J. L. Jimenez, C. P. McKay, D. R. Worsnop, O. B. Toon and M. A. Tolbert, *Geophys. Res. Lett.*, 2004, **31**, L17S08.
90 D. Dubois, N. Carrasco, J. Bourgalais, L. Vettier, R. T. Desai, A. Wellbrock and A. J. Coates, *Astrophys. J., Lett.*, 2019, **872**, L31.
91 E. Sciamma-O'Brien, C. L. Ricketts and F. Salama, *Icarus*, 2014, **243**, 325–336.
92 P. Rannou, T. Cours, S. Le Mouélic, S. Rodriguez, C. Sotin, P. Drossart and R. Brown, *Icarus*, 2010, **208**, 850–867.
93 E. Sittler Jr, A. Ali, J. Cooper, R. Hartle, R. Johnson, A. Coates and D. Young, *Planet. Space Sci.*, 2009, **57**, 1547–1557.
94 J. C. Loison, M. Dobrijevic and K. M. Hickson, *Icarus*, 2019, **329**, 55–71.
95 K. Wohlfart, M. Schnell, J.-U. Grabow and J. Küpper, *J. Mol. Spectrosc.*, 2008, **247**, 119–121.
96 B. Khare, C. Sagan, J. E. Zumberge, D. S. Sklarew and B. Nagy, *Icarus*, 1981, **48**, 290–297.

